




Smart Space Deployable Truss Based on Shape-Memory Releasing Mechanisms and Actuation Laminates

Xin Lan,^{*} Liwu Liu,[†] Chengtong Pan,[‡] Guanghua Hou,[§] Fengfeng Li,[¶] Zhengxian Liu,^{**}
Wenxu Dai,^{††} Linlin Wang,^{‡‡} Fenghua Zhang,^{§§} Jian Sun,^{¶¶} Honghao Yue,^{***} Yanju Liu,^{†††} and
Jinsong Leng^{‡‡‡} 

Harbin Institute of Technology, 150080 Harbin, People's Republic of China
and

Xiaoqing Zhong^{§§§} and Yong Tang^{¶¶¶}
Institute of Telecommunication Satellite, Chinese Academy of Space Technology, 100094 Beijing,
People's Republic of China

<https://doi.org/10.2514/1.A35649>

A structure-level smart deployable truss (SDT) was further studied for on-orbit verification on the SJ18 Geostationary Satellite in this work on the basis of a material-level validation of a shape-memory polymer composite (SMPC) sheet on the SJ17 Geostationary Satellite in 2016. In the SDT, a shape-memory alloy (SMA) mechanism was used to replace traditional pyrotechnic devices for locking and releasing, and SMPC actuation laminates were employed to replace traditional motor or spring driving mechanisms. With a strict parameter constrain of mass, size, and stiffness, the current form of the SDT flight hardware was finally obtained through several cycles of optimization design. Its systematical ground-based experiments were conducted, and the overall structural and functional performance met the demands of the aerospace standards of China. The locking force and expansion breaking force of the SMA releasing mechanism were ~2000 and ~10,000 N, ensuring the locking and unlocking reliability for the movable parts with mass 5 kg. The actuation force of all SMPC laminates decreased from ~30 N (0°) to ~12 N (165°) with a recovery duration of ~150 s, which was strong enough for SDT deployment in space. The shape-memory materials show great prospects for smart deployable structures in space.

I. Introduction

CONVENTIONAL space deployable structures mainly consist of a movable mechanism with rigid rod as well as rigid joints, and they are actuated by motors. These rigid structures enable a relatively high stiffness [1,2]. However, the complex structures are almost heavy, which leads to limited deployed dimensions [3,4]. Thin wall structure is another type of deployable structure; it could deform into a large structural reflection with small material strain [5,6]. The releasing of strain energy of a thin wall structure makes it deploy to the desired configuration. The extremely thin wall thickness (i.e., 0.1 mm [5]) enables a large packaging ratio but leads to a relatively low structural stiffness [7–9].

Conventional resin-based composites mainly concern the static or quasi-static mechanical load-bearing properties, such as stiffness and strength, and are primarily used for structural materials. The tensile strain limit of the carbon-fiber-reinforced composites is ~0.8–1.4% [10–13], and the compressive strain limit is ~0.8% [14]. A soft material may show as high as 10–100% large deformation, but its stiffness is low and is unable to be used for load bearing. If the load-bearing, large-deformation, and driving characteristics can be realized through one material, it would show great prospects [15–17]. Fiber-reinforced shape-memory polymer composites (SMPCs) not only show structural load-bearing performance but also have functional characteristics, such as large deformation and driving, compared with conventional resin-based composites [18,19]. When a shape-memory polymer (SMP) is far below its glass transition temperature T_g , the elastic modulus and strength are at the same order of magnitude as conventional composites. Above its T_g , SMP significantly deforms on a magnitude of 100%. Based on the large deformation of SMP and buckling deformation of carbon fibers, a maximum macroscopic compressible strain of approximately 8–10% can be obtained [20–23]. Regarding the deformation mechanism of SMPC, the expressions of key parameters in large bending deformation process were derived [20,21], including critical curvature, wavelength and amplitude of the buckling fiber, key macroscopic strains of the SMPC, and driving torque. Based on the above theories, a design method of the SMPC large deformation structure is formed.

Received 22 December 2022; revision received 0 ; accepted for publication 29 December 2022; published online 25 January 2023. Copyright © 2023 by the American Institute of Aeronautics and Astronautics, Inc. All rights reserved. All requests for copying and permission to reprint should be submitted to CCC at www.copyright.com; employ the eISSN 1533-6794 to initiate your request. See also AIAA Rights and Permissions www.aiaa.org/randp.

^{*}Associated Professor, Center for Composite Materials and Structures; lanxin@hit.edu.cn. Equally Contributed with Second Author.

[†]Professor, Department of Astronautical Science and Mechanics, P.O. Box 301, No. 92 West Dazhi Street; liuliwu_006@163.com. Equally Contributed with First Author.

[‡]Ph.D. Student, Center for Composite Materials and Structures; pct1136144344@163.com.

[§]Ph.D. Student, Department of Astronautical Science and Mechanics, P.O. Box 301, No. 92 West Dazhi Street; houbaozhua@126.com.

[¶]Post-Doctoral Fellow, Department of Astronautical Science and Mechanics, P.O. Box 301, No. 92 West Dazhi Street; eastlifelifengfeng@126.com.

^{**}Ph.D. Student, Department of Astronautical Science and Mechanics, P.O. Box 301, No. 92 West Dazhi Street; liuzhengxian_hit@qq.com.

^{††}Engineer, Department of Astronautical Science and Mechanics, P.O. Box 301, No. 92 West Dazhi Street; 1241549917@qq.com.

^{‡‡}Ph.D. Student, Center for Composite Materials and Structures; wangll_hit@163.com.

^{§§}Associated Research Fellow, Center for Composite Materials and Structures; fhzhang_hit@163.com.

^{¶¶}Professor, Center for Composite Materials and Structures; sunjianhit@163.com.

^{***}Professor, School of Mechatronic Engineering; yuehonghao@hit.edu.cn.

^{†††}Professor, Department of Astronautical Science and Mechanics, P.O. Box 301, No. 92 West Dazhi Street; yj_liu@hit.edu.cn.

^{‡‡‡}Professor, Center for Composite Materials and Structures; lengjs@hit.edu.cn (Corresponding Author).

^{§§§}Senior Engineer, P.O. Box 5142, No. 104 Youyi Street, Haidian District; hitxq@126.com.

^{¶¶¶}Senior Engineer, P.O. Box 5142, No. 104 Youyi Street, Haidian District; txwx_tangyong@163.com.

The SMPC structures can be designed with appropriate thickness, bending curvature, and fiber volume content, according to functional requirements, such as deformation and driving force [21]. In this way, the reasonable wall thickness (i.e., 1 mm) and simple structural form of SMPC combine the advantages of conventional deployable mechanisms and thin wall deployable structures. An SMPC is a prospective candidate for developing new-generation deployable structures in space.

In recent years, the applications of SMPCs in space deployable structures have received extensive attention owing to their variable stiffness and large deformation characteristics. Some principle verifications of SMPC-based components were completed and even further applied in realistic engineering [22,23]. DSX/PowerSail developed a new generation of large-area, lightweight, and high-energy solar panels, relying on longitudinally extending tubular SMPC beams [24]. Considering the shape transformation, the SMPC beam was a rolled tape in storage state and transformed to a straight tubular beam with a “C”-shaped cross section to obtain a relatively high stiffness [24]. Moreover, SMPC deployable hinges were used to deploy an experimental solar panel on TacSat-2 satellite, and the recovery force was experimentally tested in the International Space Station (ISS) in 2007 [25]. In 2007, a SMPC gravity gradient boom was developed with a 3.3 m length and 8 kg tip mass and was validated on microsatellite demonstration mission FalconSat-3 [23,26,27]. This SMPC gravity gradient deployable boom showed lower densities, higher strain capacities, and higher damping capabilities over shape-memory alloys or ceramics. The material-level shape recovery behaviors of the SMP foam have been also tested in the Shuttle Mission STS-134 in the ISS in 2011 [28], and Mission BION-M1 of the Soyuz spacecraft in 2013 [29]. A 100% recovery ratio of the SMP foam was difficult to obtain because its recovery force was low. In 2012, the shape-memory recovery performance of the SMP sheets was evaluated in Japan Experiment Module in the ISS [30], and the electrical heating was used to trigger the recovery deformation. A large-scale deployable reflector structure was designed by Jet Propulsion Laboratory, and the SMPC hinges were employed for the reflector back frame structure to realize the deployment actuation [31]. A deployable lunar housing structure was developed with a length of 32 feet and a diameter of 16 feet. This large inflatable pressure structure was composed of a multilayer structure, and the main support frame was made of SMPC [32]. In 2016, the shape-memory effect of a carbon-fiber-fabric-reinforced SMPC laminate was verified on the SJ17 Geostationary Satellite, and the long-term material stability resistance to spatial radiation and vacuum was validated [33]. The research on SMPs and SMPCs is expected to promote the development of smart active deformation structures

on aerospace vehicles, such as space deployable hinges and smart solar arrays.

The pyrotechnic separation device is a mechanism used for connection, locking, and separation of aerospace vehicles, and it is widely used in the separation of satellites and rockets and payload release. The explosive shock produced by the pyrotechnic separation device is one of the harshest mechanical environments experienced by almost all spacecraft, and the transient acceleration amplitude of the explosive shock could reach as large as 10,000 g [34]. Pyrotechnical shock loads may cause damage to instruments and equipment containing shock-sensitive components and brittle materials (e.g., crystal oscillators, ceramics, relays, brazing, and microelectronic chips), resulting in the failure of space missions and even a catastrophic accident [35]. In addition, the pyrotechnic separation device can only be used once; therefore, a single pyrotechnic product is not testable. The harmful gas generated during the combustion or explosion may pollute the space environment, such as lens and electronic devices [36]. Therefore, nonpyrotechnics connection unlocking technology must be urgently developed to overcome the shortcomings of traditional pyrotechnics. Shape-memory alloy (SMA) intelligent locking and releasing mechanisms were developed using SMA's high rigidity and shape-memory active large deformation characteristics [37–39]. These devices showed the advantages of small volume and weight, low unlocking impact load, high recyclability, no pollution, and high reliability [40,41].

The smart deployable truss (SDT) was studied in this work based on the material-level verification of a small SMPC laminate on the SJ17 Geostationary Satellite on a geostationary orbit in 2016 [33]. The SMA releasing mechanism was used to replace traditional pyrotechnic devices for locking and releasing. Meanwhile, the carbon-fiber-reinforced SMPC actuation laminates were employed to replace traditional motor or spring driving mechanisms. The SDT was strictly designed, optimized, simulated, and ground-based tested according to the aerospace standards of China. The optimization design process of the SDT has been published in our previous paper [42]. In this paper, we intensively introduce the whole project of SDT, including the overall design and analysis, the whole system of ground-based experiments, and the verification of locking function in the initial launching process. Due to the unfortunate failure of Long-March Five Y2 Rocket, the originally planned content is missing, namely, on-orbit releasing and deployment verification.

II. Structural Design of the SDT

A. System Design of the SDT

As shown in Fig. 1, the SDT consists of three types of parts: 1) metallic structural frames (metallic chassis, support frame, central

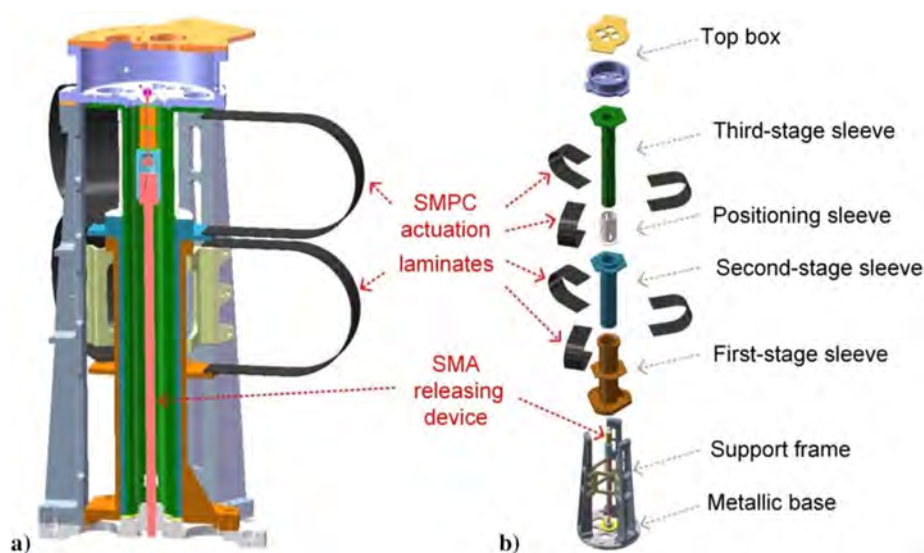


Fig. 1 Structural design of the SDT: cross-sectional view (a) and explosive view (b).

moveable sleeves, and top box); 2) SMPC actuation laminates; and 3) SMA releasing mechanism.

The function and typical working process of the SDT can be summarized into three steps:

1) During ground transportation and launching, the SDT is pre-tightened by an SMA releasing mechanism to maintain the structural integrity and reasonable stiffness of the SDT (Figs. 1 and 2a). The SMA releasing mechanism is in a prestretched state, while the following parts are in precompressive state, including three sleeves, positioning sleeve, and support frame. The SMPC actuation laminates are folded and contracted into U shapes. The first-stage SMPC actuation component consists of three SMPC laminates with 120° apart, which connects with the first-stage and second-stage sleeves. The second-stage SMPC actuation component has the same structure, which is connected with the second-stage and third-stage sleeves.

2) During a deployment process on-orbit, the SMA releasing mechanism breaks into two parts upon electrical heating to release the moveable parts, including second-stage sleeve, positioning sleeve, third-stage sleeve, and top box. Thereafter, the two stages (six pieces) of the SMPC actuation laminates are electrically heated and recover from the U shape toward a flat shape due to the shape-memory effect (Fig. 2b). The adjacent sleeves relatively slide until the spring locking pins are triggered due to the actuation of the SMPC laminates. Then, the SDT deploys into a designed configuration.

3) In a deployed state on-orbit, the payload on the top box works at the designed position. The deployed SDT can also present reasonable axial stiffness due to the spring locking pins between the adjacent sleeves and high lateral stiffness due to the reasonable wall thickness

and overlap region between the adjacent sleeves. Note that, readers could also find more details about the structural design of SDT in our previous study [42], which particularly discussed the structural optimization of SDT.

The optimization design of the SDT was constrained with the main parameters: mass (≤ 12 kg); height in folded and deployed shapes (≤ 0.5 and ≥ 1 m); fundamental frequencies in folded and deployed shapes (≥ 120 and ≥ 4 Hz); structural safety in the $8g$ vibration condition. The structure of the SDT was optimized in several cycles of design, finite element analysis (FEA), and experimental tests, as illustrated in Fig. 3. Several critical points on the bases of the first-stage sleeve of the SDT were chosen to evaluate the stress status during the FEA and experiments. The contact stiffness between adjacent two parts of SDT was difficult to be specified in the first-step FEA; hence, they were artificially adjusted according to the resonance frequency of the experimental results. In addition, the finite element method (FEM) model should be correlated with those of the experimental results at least three orders of resonance frequencies and the stress values at selected critical points of the original structure design. Based on this correction FEM model, more strength and vibration information could be further obtained and analyzed to ensure the safety of the SDT in serious vibration conditions. Then, a structural optimization design model could be further provided, and the next-step experimental validation was carried out. In summary, the whole steps of the study and verification for the SDT can be summarized as follows: original structural design, FEM model analysis, first-step fabrication and experimental testing in the $12g$ vibration condition, correction and optimized FEM model modifications,



Fig. 2 Structural design of the SDT in a folded shape (a) and in a deployed shape (b).

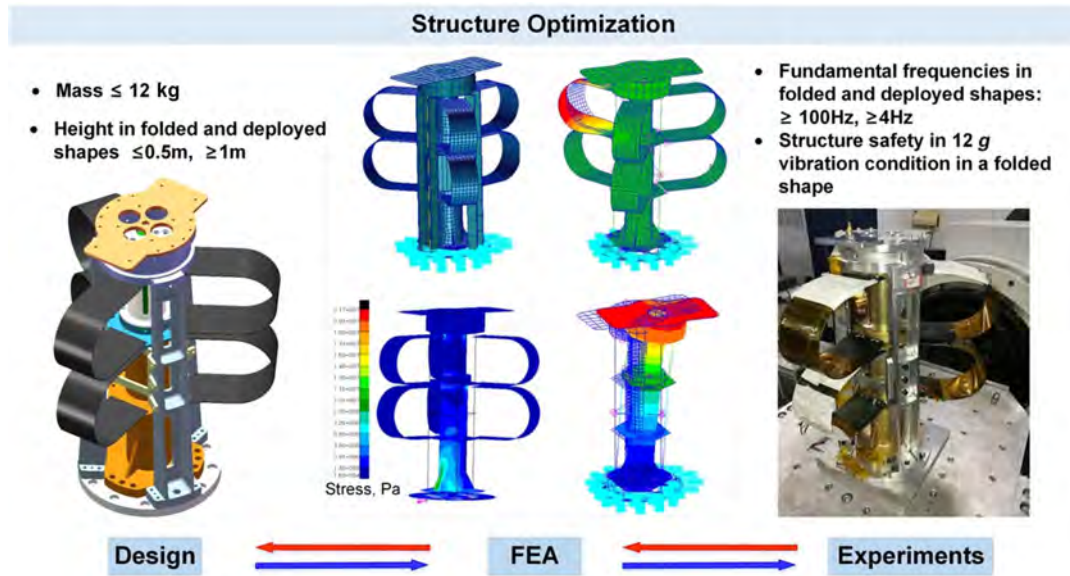


Fig. 3 Schematic illustration of the structural optimization of the SDT.

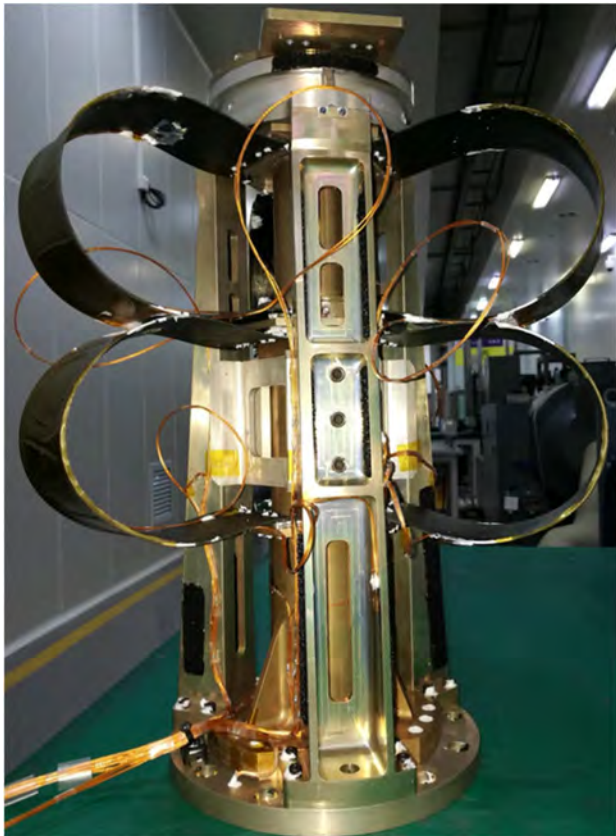


Fig. 4 SDT flight hardware for on-orbit evaluation aboard the SJ18 Geostationary Satellite.

last-step design optimization, fabrication and experimental testing, last-step fabrication and ground-based experimental verification in the 8 g vibration condition, launching with the SJ18 Geostationary Satellite, locking and releasing verification on-orbit, deployment verification on-orbit, and long-term on-orbit verification. Given that the structural design of the SDT has been described in detail in our previous study [42], the detailed process and results were excluded in this work, which intensively introduces the whole project of SDT. At least three cycles of structural design, FEA, and ground-based experiment were carried out to obtain the final form of the SDT flight hardware, as shown in Fig. 4.

Table 1 Main parameters of the structure and function of the SDT

Parameter	Value
Mass, kg	11.2
Configuration	Two-step deployment
Envelope size in a folded state, mm	490 × Φ415
Envelope size in a deployed state, mm	970 × Φ310
Fundamental frequency of a deployed main structure, Hz	126
Heating power for an SMA releasing mechanism, W	~38
Pretensioning force of an SMA releasing mechanism, N	~2000
Unlocking duration of an SMA releasing mechanism, s	30 ± 2
Deployment duration of the SMPC laminates, min	<3
Heating power for one SMPC laminate, W	~79
Fundamental frequency of a deployed main structure, Hz	5.3
Design life of the SDT on-orbit, year	>2

The main parameters of the structure and function of the SDT are listed in Table 1. The total mass of the SDT was 11.2 kg, with an envelope size of height 490 mm and diameter 415 mm in a folded state and height 970 mm and diameter 310 mm in a deployed state. The fundamental frequency of the main structure of the SDT in a folded state was 126 Hz with a relatively high locking stiffness of the SMA releasing mechanism. The SDT was released within approximately 30 s with an electrical heating power of 38 W for the SMA releasing mechanism and deployed within 3 min with a stepped electrical heating power of 237 W for the SMPC actuation laminates. The shape recovery ratio of the SMPC actuation laminates was approximately 90–95%. The fundamental frequency of the main structure of the SDT in the deployed state was approximately 126 Hz due to the structural design of the deployed SDT with relatively high stiffness, which met the mechanical demands of the aerospace standards of China.

B. SMA Releasing Mechanism

The SMA releasing mechanism provided pretightening for the SDT structure in ground-based testing and launching. As shown in Fig. 5, the SMA releasing mechanism consists of an SMA expansion mechanism (SMA expansion breaker, grooving titanium rod, polyimide electric heating film, housing, and heat insulation pad), a pretightening cylinder barrel, a pretightening long rod, a pretightening ball head, a pretightening pad, and a pretightening nut.

In a locking state, the bottom plate of the moveable top box was connected with the metallic chassis through the pretightening SMA releasing mechanism. In this way, all the other moveable parts

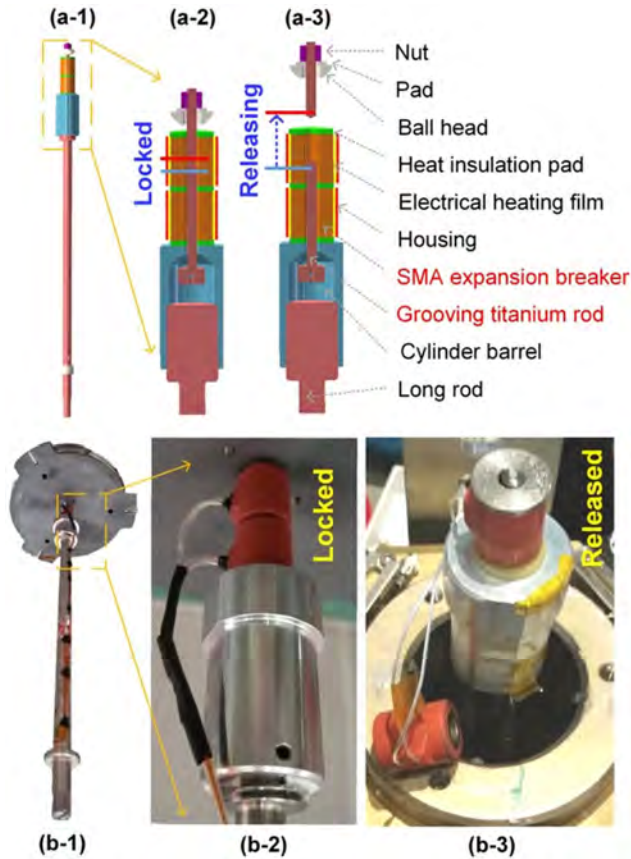


Fig. 5 Structural design and physical objects of the SMA releasing mechanism.

(second-stage sleeve, positioning sleeve, third-stage sleeve, and SMPC actuation laminates) were tightly locked onto the SDT metallic chassis, which is connected to the satellite desk. The transmission pathway of the pretightening stretching force is listed in sequence as follows: bottom plate of the top box, grooving titanium rod, cylinder barrel, pretightening long rod, and metallic chassis. The mechanical parameters (prestretched stress and the corresponding grooving dimensions) of the grooving titanium rod were accurately designed, which connected the top box and the cylinder barrel. The pretightening force could be adjusted by the nut on the bottom plate of top box. Two SMA expansion breakers were mechanically connected in a series to improve the reliability of the releasing function of the SMA releasing mechanism. In this case, the SMA releasing mechanism could release the SDT in a normal manner even when only one SMA expansion breaker worked.

The SMA expansion breaker (Table 2) was hollow cylindrical in shape, which was TC4. The typical mechanical characteristics of TC4 were ≥ 1104 MPa tensile strength, ≥ 1000 MPa residual elongated stress, $\geq 10\%$ elongation rate, and $\geq 20\%$ section shrinkage. Regarding shape-memory effect, the TC4 also showed the following

characteristics: with up to 4% strain and no less than 344.7 MPa recovering stress.

The SMA expansion breaker was precompressed with approximately 4% strain. The prestretching force for an SMA expansion breaker was designed to be ~ 2000 N. The total mass of the moveable parts of the SDT is less than 5 kg (~ 50 N), and the maximum acceleration during launching for a spacecraft is less than 10 *g*. Hence, the limit value of the vibration inertial force of the moveable parts during launching was 500 N. Based on the above parameters, the coefficient of the locking safety margin of the SDT is larger than four (i.e., $2000 \text{ N}/500 \text{ N} = 4$). The two electrical heating films were connected in a series. The resistance of a single electrical heating film of the SMA expansion breaker was 20Ω with a power of 19.2 W. The recovery expansion force of each SMA hollow cylinder was $\sim 10,000$ N, where the coefficient of the releasing safety margin of the SDT is approximately five (i.e., $10,000 \text{ N}/2000 \text{ N} = 5$).

During releasing, when the temperature of the SMA expansion breaker reached its transition temperature upon electrical heating, the hollow SMA cylindrical expanded, and the grooving titanium rod was forced to expand, and finally broke (Figs. 5a-3 and 5b-3). Accordingly, the pretightening ball head moved away from the bottom plate of the tip box, and all the moveable parts were free in their respective movement directions. The SDT would deploy to a desired configuration due to the subsequent actuation of the SMPC laminates. The SMA expansion breaker was able to work in -50 to 60 °C with a ground storage duration of ≥ 2 years and a space storage duration of ≥ 3 months.

C. SMPC Actuation Laminates

The fiber-reinforced SMPC laminates could perform as large as 8–10% macroscale compression deformation due to the local microbuckling deformation of reinforced fibers. Meanwhile, the SMPC structures exhibit large bending deformation. The large bending deformation of an SMPC laminate could be divided into three stages: nonbuckling stage with a small bending deformation, post-microbuckling and actuation function stage, and buckling failure stage with an extremely large deformation. A super small curvature radius-to-thickness ratio for the fabric-reinforced SMPC could be obtained due to the microbuckling array of the carbon fiber tows. The SMPC laminates could actuate the moveable sleeves of the SDT according to this large deformation characteristics and shape-memory effect.

As shown in Fig. 6, the SMPC actuation laminates were primarily fabricated by the cyanate-based SMP and carbon fiber fabrics. The cyanate-based SMP is a class of binary phenol derivatives containing two or more cyanate ester functional groups with a general formula $\text{N}\equiv\text{C}-\text{O}-\text{Ar}-\text{O}-\text{C}\equiv\text{N}$. Under the action of heating and catalyst, a thermosetting cyanate-based SMP can be prepared based on our previous study [44]. Thiothiazinone formed in the reaction gives the material a 3D network cross-linking structure. A dynamic mechanical thermal analysis was conducted. The result showed that the glass transition temperature T_g of the pure cyanate ester SMP was approximately 200°C , and the storage modulus was 1.73 GPa at 20°C . The tensile modulus and strength at 25°C were 1.95 ± 0.04 GPa and 65.5 ± 1.2 MPa, respectively. The T_g of the SMPC was approximately 200°C . The storage modulus was ~ 5 GPa at room temperature, and ~ 300 MPa at the glass state above T_g [42]. The reinforcement of the SMPC actuation laminate was a carbon-fiber twill weave fabric (T300-3K, Toray, Japan). The typical parameters are 230 GPa tensile modulus, 3530 MPa tensile strength, 1.5% limit of elongation rate, and 1.8 g/cm^3 density. The vacuum-assisted resin transfer molding (VARTM) [44,45] was used to fabricate the SMPC laminates. Four layers of carbon fiber twill weave fabrics were included for each piece of the SMPC laminate, with approximately 53% volume fraction of reinforcement. The dimensions of the first-stage and second-stage SMPC laminates were $394 \text{ mm} \times 70 \text{ mm} \times 1.5 \text{ mm}$ and $378 \text{ mm} \times 70 \text{ mm} \times 1.5 \text{ mm}$, respectively.

The SMPC laminates were the actuation parts for the SDT deployment. There were six pieces of SMPC actuation laminates, which were divided into two groups, as shown in Fig. 2a. A piece

Table 2 Main parameters the structure and function of SMA expansion breaker

Parameter	Value
Material	TC4 (Ti–6Al–4V)
Transition temperature, °C	80
Ratio of heat, J/(kg · °C)	322
Latent heat, J/kg	24,200
Young's modulus, GPa	75
Yield strength (austenite), MPa	551
Yield strength (martensite), MPa	103
Tensile strength, MPa	758–965
Elongation rate, %	15
Poisson's ratio	0.31

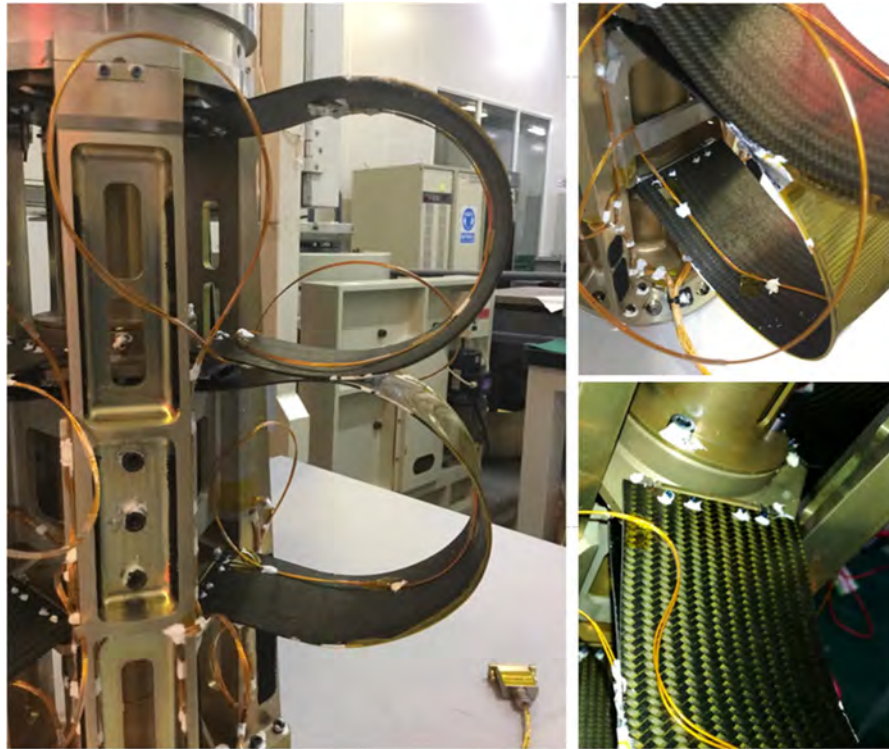


Fig. 6 SMPC laminates installed on the SDT as actuation parts.

of electrical heating film was attached on one side of each SMPC laminate. The resistance of a single electrical heating film of an SMPC actuation laminate was approximately 127Ω with a power of 79 W. During the ground-based operation, all the six pieces of SMPC laminates became soft when the temperature was above T_g due to the electrical heating by the direct current. Subsequently, all the central moveable sleeves were compressed to the locking state and pretightened by adjusting the pretightening nut on the bottom plate of the top box. All the SMPC laminates were compressed into a U shape. Then, upon switching off the current, the SMPC laminates recovered to be hard for experiments and ground transportation of SDT. After the SDT launched aboard the satellite and flew on-orbit, the SMA releasing mechanism first released the moveable parts. Second, all the SMPC laminates were heated to actuate all the moveable parts to the desirable positions. Then the self-locking pins would work to maintain the deployed configuration and structural stiffness.

D. Support Frame and Central Moveable Sleeves

The support structure consists of three support beams and three cages. The variable cross-sectional beams were obtained by undergoing an optimization design of the support beams by combining the strength and vibration. One microswitch was installed on the tip of one support beam. Once the top box was released by the SMA releasing mechanism and actuated by the SMPC laminates, the microswitch would be triggered. The corresponding phase step signal would be transferred to the Earth through the SJ18 Satellite. Given that the deployment movement of SDT was along the perpendicular direction to the desk of satellite, the stepwise moveable rod-fashion sleeves were designed. Meanwhile, the movement in the lateral direction was constrained. The central moveable sleeves consisted of three stages of sleeve. The spring positioning pin structures were designed on the sleeve to locking the deployment state and ensure the deployment stiffness for SDT.

III. Ground-Based Experiments and Evaluation of the SDT

Systematical ground-based experiments have been carried out, and the overall structural and functional performances have been

evaluated to ensure the safety and reliability of SDT. The structural mechanics performance of SDT (i.e., sinusoidal sweep and random vibration test, shocking test, and acceleration test) was tested to evaluate its strength and vibration behavior. The temperature condition was essential for SMA and SMPC because they are thermal responsive materials. The thermal design of SDT and the associated experiments in simulated vacuum conditions were necessary. The locking and releasing performance of the SMA releasing mechanism of SDT was also evaluated. The actuation performance of the SMPC laminates as the actuation parts was tested in various conditions, including varying ambient temperatures, thermal design scheme with different heat insulation multilayer components, and varied electrical-heating duration. Finally, the integrated test was performed to evaluate the ground-based releasing and deployment performance of the SDT.

A. Structural Mechanics Tests

1. Sinusoidal Sweep and Random Vibration Tests

Sinusoidal sweep and random vibration tests were performed to evaluate the resonance characteristic under special external excitation. The vibration was controlled in the displacement mode (5 mm) for the sinusoidal sweep test in the frequency range of 5–20 Hz. The vibration was controlled in the acceleration mode (8 g) in the frequency range of 20–100 Hz with a sweeping velocity of 4 oct/min. The corresponding vibration amplitudes for the random vibration test in the frequency ranges of 20–100, 100–600, and 600–2000 Hz were +6 dB/oct, $0.1 g^2/\text{Hz}$, and -12 dB/oct , respectively. The acceleration root-mean-square values of the random vibration test were also 8 g. In addition, the characteristic sinusoidal sweep with a vibration amplitude of 0.2 g was carried out before and after each normal vibration test to test the frequency responses. Accordingly, the variation of the structural stiffness of SDT was determined. The main procedure for the vibration tests in the X direction on the three-axis slip table as shown in Fig. 7 was listed as follows: 0.2 g characteristic sinusoidal sweeping, 8 g sinusoidal sweeping, 0.2 g characteristic sinusoidal sweeping, 8 g random vibration, and 0.2 g characteristic sinusoidal sweeping. Then, the vibration tests were carried on in the Y and Z directions with the same procedure as the X direction.

The frequency response results of SDT in 0.2 g characteristic sinusoidal sweep vibration tests are presented in Fig. 8 as an

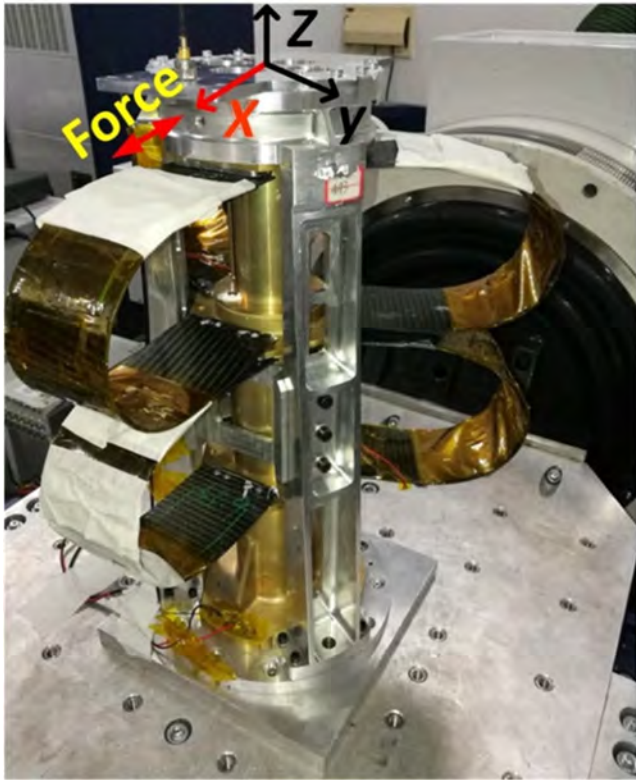


Fig. 7 Sinusoidal sweep and random vibration tests of the SDT in the X direction on a slip table.

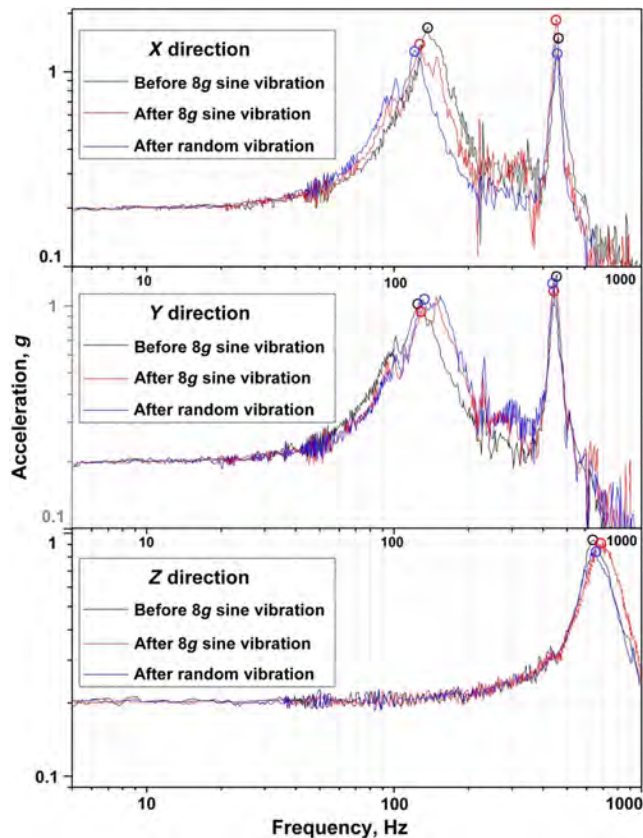


Fig. 8 Frequency responses of the SDT with 0.2 g characteristic sinusoidal sweep vibration tests.

important indicator to reflect the structural stiffness variation of the SDT undergoing vibration condition. Three frequency response curves were given in each experimental direction of the SDT, namely,

before the 8 g sweep vibration test, after the 8 g sweep vibration test, and after the random vibration test. In the X and Y directions, the SDT showed similar trend and values of the frequency response curves because the main frame of the SDT was circumferential symmetry in the X–Y plane. There were two peak areas (i.e., ~ 130 and ~ 450 Hz) that represent the first-order and second-order resonance frequencies in the X and Y directions. In the Z direction, there was only one peak area (i.e., ~ 650 Hz), indicating the first-order resonance frequencies. The data before and after the 8 g sine vibration in Fig. 8 were referenced from our previous paper [42], which particularly discussed the structural optimization.

Table 3 lists the resonance frequencies and the corresponding acceleration amplitudes of the SDT under various experimental conditions. The first-order resonance frequency in the X direction was 137.20 Hz before the 8 g sinusoidal vibration and then reduced to 127.95 Hz (after the 8 g sinusoidal vibration) and 121.13 Hz (after the random vibration). The contacting stiffness slightly decreased due to the local slight deformation on the contact surface between the adjacent parts undergoing vibration, and a frequency drop (from 137.20 to 127.95 Hz) just after the 8 g sinusoidal vibration test was evident. Then, the contact stiffness became stable, and the first-order resonance frequencies maintained at a relatively stable values, namely, 121.13 Hz after the random vibration in the X direction and 126.40–131.11 Hz in the Y direction. The second-order resonance frequencies were stable and maintained in the range of 447.26–462.23 Hz. The first-order acceleration resonance amplitudes in the X and Y directions were in the range of 0.94–1.72 g, with a dynamic magnification factor of 4.7–8.6. The second-order acceleration resonance amplitudes were in the range of 1.25–1.87 g, with a dynamic magnification factor of 6.25–9.35. The first-order acceleration resonance frequencies for the vibration in the Z direction were concentrated in range of 641.75–665.64 Hz.

During the launching of the SJ18 Satellite, the external excitation applied on the SDT would be random force. The frequency response curves of the random vibration are provided in Fig. 9 and Table 4. The aforementioned curves were also similar with those in the X and Y directions. The first-order resonance frequencies were 126.15 Hz (X direction) and 126.92 Hz (Y direction), and the second-order resonance frequencies were 452.36 Hz (X direction) and 402.10 Hz (Y direction), which correlated with the resonance frequencies of the 0.2 g sinusoidal sweep vibration tests. The first-order resonance frequency in Z direction was 438.70 Hz. The first-order acceleration resonance amplitudes were 3.31 g (X direction), 3.19 g (Y direction), and 1.97 g (Z direction). The second-order acceleration resonance amplitudes were 0.43 g (X direction) and 0.40 g (Y direction).

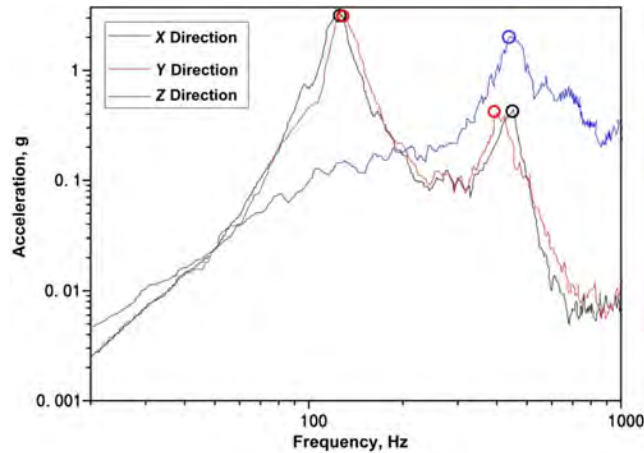
The frequency responses of the SDT in a deployed state were tested. The SDT's dimensions were 970 mm in height and 310 mm in diameter. The hammer strike method was employed to record the transient excitation force and vibration responses. The three-axis accelerometer was placed on the top surface of the top box to collect the acceleration response data. The frequency responses were calculated to indicate the frequency characteristics. Based on the results, the first resonance frequency was 5.371 Hz, which was higher than the designed demand of ≥ 4 Hz.

2. Shocking Test

The transient shocking test was necessary to evaluate the structural safety and reliability of the SDT undergoing ground transportation and launching (Fig. 10). The shocking amplitude values in the ranges of 100–1500 and 1500–4000 Hz were +6 dB/oct and 800 g, respectively. At least 50% of the impact response spectrum should be greater than the rated test standard value. The transient shocking test was carried out in the X, Y, and Z directions, with only one shocking test in each direction. Figures 11a–11c provide the time domain curves of the shocking acceleration tests in three directions. Considering the characteristics of the time domain, the impacting response durations were approximately 20 μ s. According to the shocking response spectrum, the maximum response amplitude was approximately 500 g. After these shocking tests, the appearance of structure and the locking state of the SMA releasing mechanism were normal.

Table 3 Resonance frequencies and acceleration amplitudes of the SDT in the 0.2 g characteristic sinusoidal sweep vibration tests

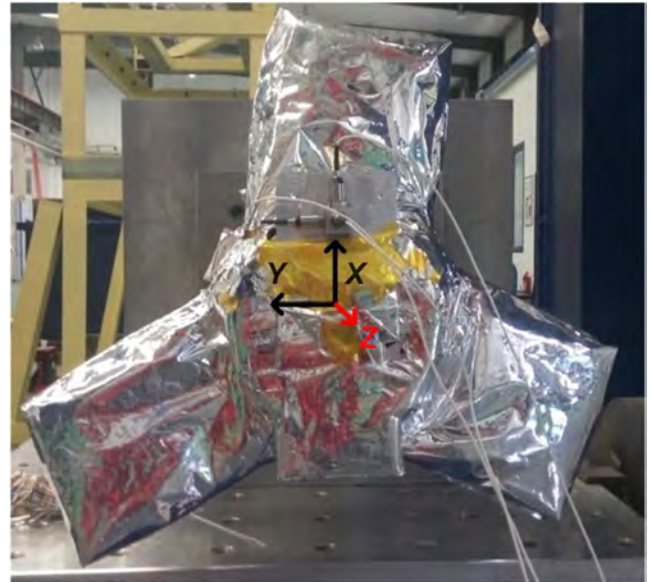
Direction	Order of resonance	Parameter	Before the 8 g sinusoidal vibration	After the 8 g sinusoidal vibration	After the random vibration
X	First order	Frequency, Hz	137.20	127.95	121.13
		Acceleration, g	1.72	1.34	1.29
	Second order	Frequency, Hz	458.80	450.75	462.63
		Acceleration, g	1.51	1.87	1.29
Y	First order	Frequency, Hz	126.40	128.73	131.11
		Acceleration, g	1.04	0.94	1.06
	Second order	Frequency, Hz	450.49	446.52	447.26
		Acceleration, g	1.37	1.25	1.27
Z	First order	Frequency, Hz	641.75	665.64	653.58
		Acceleration, g	0.93	0.92	0.85

**Fig. 9** Frequency responses of the SDT in the random vibration tests (vibration amplitude: root-mean-square values of 8 g).**Table 4** Resonance frequencies and acceleration amplitudes of the SDT in the random vibration tests (vibration amplitude: root-mean-square values of 8 g)

Direction	Order of resonance	Parameter	Value
X	First order	Frequency, Hz	126.15
		Acceleration, g	3.31
	Second order	Frequency, Hz	452.36
		Acceleration, g	0.43
Y	First order	Frequency, Hz	126.92
		Acceleration, g	3.19
	Second order	Frequency, Hz	402.10
		Acceleration, g	0.40
Z	First order	Frequency, Hz	438.70
		Acceleration, g	1.97

3. Acceleration Test on a Centrifuge

Acceleration test was used to evaluate the structural safety and reliability of the SDT under the acceleration condition during the launching of Long-March Five Y2 Heavy Rocket. Some thin film parts (e.g., thermal insulation multilayers of the SDT and electrical heating films attached to the SMPC actuation laminates) might tear due to large elongation or twist deformation upon applying a high-level overload. The acceleration test was carried out on a centrifuge with an arm length of 4 m, which was five times larger than the dimensions of SDT, as shown in Fig. 12. It was tested in three directions by changing the X, Y, or Z direction of the SDT along the direction of the centrifugal force. The accelerating rate of the centrifuge was 3.5 g/min, and the simulated acceleration was 10.5 g with an examining duration of 5.2 min. During the acceleration testing, the appearance of the SDT was normal. After the testing, all the parts of the SDT were inspected

**Fig. 10** Transient shocking test of the SDT in the Z direction.

and found to be normal, especially for the thermal insulation multilayers of the SDT, electrical heating films, and microswitches. The results indicated that the structure of SDT was safe under static or quasi-static acceleration mechanical condition.

B. Thermal Design and Experiments in the Simulated Vacuum Condition

The SDT was installed on the SJ18 Satellite in a geostationary orbit at a height of approximately 36,000 km. On this orbit, the extreme temperature range of parts, which are directly exposed to space without any protective measures, might be from -170 to $+170^{\circ}\text{C}$. The atmospheric temperature near the SMA should not be higher than 60°C to ensure the locking stability and safety because the transition temperature of SMA was 80°C . Once the temperature of SMA increased beyond 60°C , the shape-memory effect would gradually stimulate. In this way, the releasing action of the SMA releasing mechanism would be automatically triggered out of human control, which should be strictly avoided to ensure the safety of the satellite. The considerably low temperature of the SMA and SMPC should also be avoided to ensure that they can be heated as expected when applying special direct currents on the electrical heating films attached to the SMA expansion breaker and the SMPC laminates. Therefore, some thermal isolation measures had to be considered to maintain a reasonable atmospheric temperature for the SDT. Considering the locking safety of the SMA releasing mechanism and actuation reliability of the SMPC laminates, the design goal of the local atmospheric temperature of SDT was -100 to $+60^{\circ}\text{C}$.

According to the configuration and flight orbit parameters of the SDT, the incident heat flow (solar radiation, Earth albedo, and

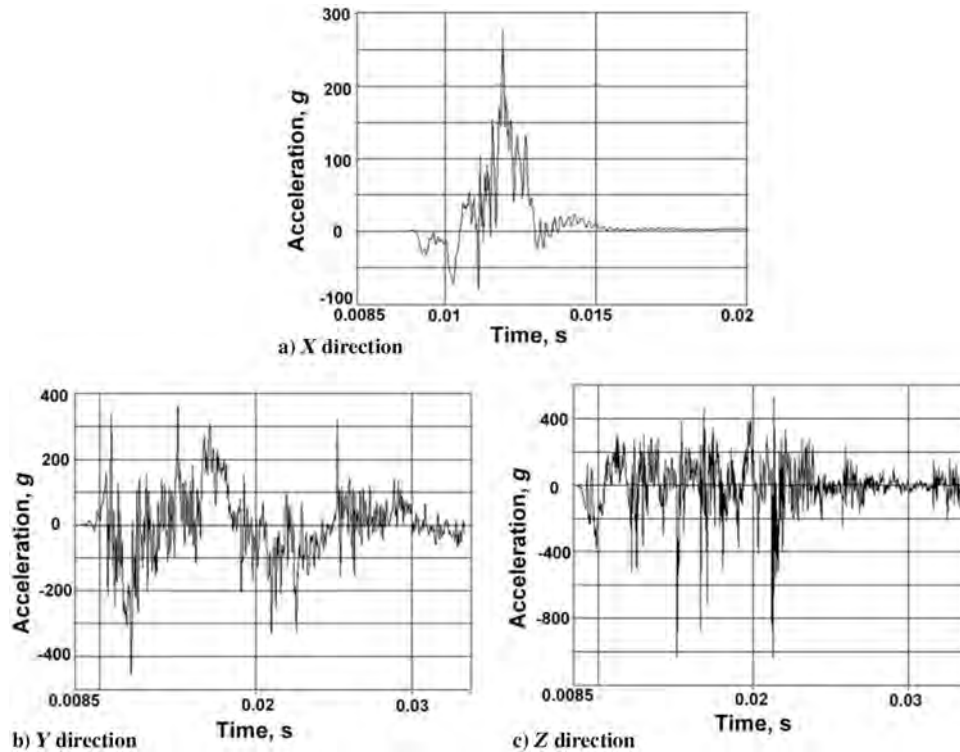


Fig. 11 Transient shocking response of the SDT in three directions.

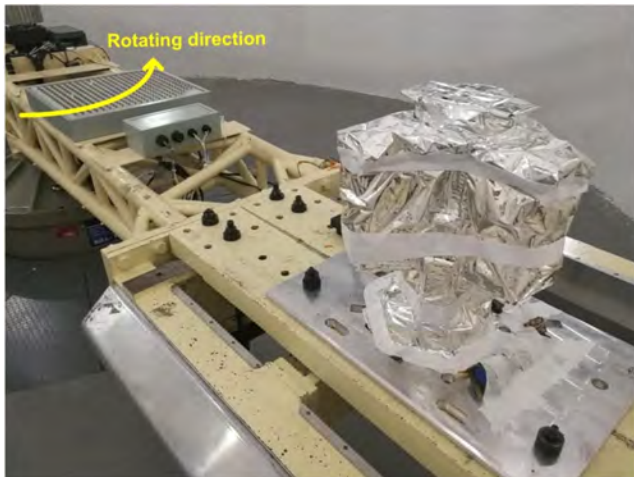


Fig. 12 Acceleration test of the SDT flight hardware on a centrifuge.

Earth infrared radiation) was calculated under three types of conditions, namely, high temperature, low temperature, and long-term facing up to the sun. The solar radiation heat flux density was 1414 W/m^2 , and the installation surface temperature was 45°C . Considering these thermal conditions, the thermal isolation measures were employed (Fig. 13), including the multilayer heat insulation assembly (HIMA) and the heat insulation pads. The HIMA consisted of five multilayer units, namely, one outer surface and four inner units. The outer surface of HIMA was an F46 film, which possessed a low solar radiative absorption coefficient (0.18) and a high solar radiation emission coefficient (0.69), to prevent heat absorption of parts on satellite. A double-sided aluminum-plated film with low emissivity and polyester mesh spacers with low thermal conductivity were used for each unit of the inner four units of HIMA to prevent heat dissipation of parts on satellite. In addition, eight heat insulation pads, which were made of polyimide with a low thermal conductivity, were installed between the metallic base and the satellite. The HIMA installed on the top box would move with top box after the unlocking of the SMA releasing

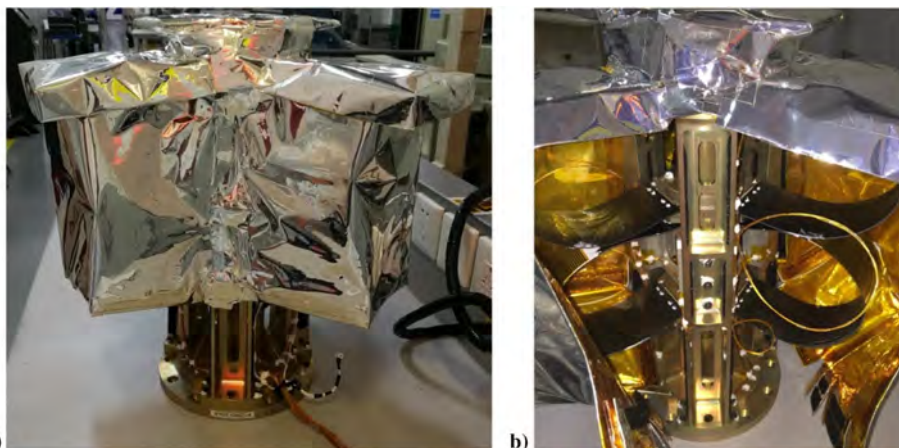


Fig. 13 Flight hardware of the thermal isolation measures of the SDT: heat insulation multilayer assembly.

mechanism. The HIMA installed on the metallic chassis and support frame was static relative to the satellite.

A thermal balance experiment and thermal cycling evaluation of the SDT coated with HIMA should be carried out to evaluate the performance of the thermal design. The results of the thermal balance experiment indicated that the extremely high temperature in a thermal balance state was approximately 47°C. The extremely low temperatures of the several testing points in the thermal balance state were approximately -80 to -120°C. Considering the design margin and reliability, the high temperature values of the thermal vacuum cycling evaluation without HIMA was specified as 13°C higher than the high temperature limit of the thermal balance experiment, namely, 60°C. The actuation of the SMPC laminate and unlocking properties of the SMA releasing mechanism were triggered at approximately 25°C atmospheric temperature at a selected orbit position. Consequently, the low temperature simulation showed a relatively weak relationship with the unlocking and actuation reliability. In this way, the low temperature value of the thermal vacuum cycling evaluation was specified as -95°C to approximately simulate the low atmosphere temperature. The main test parameters of the thermal vacuum cycling in a space environment simulation equipment were $\leq 6.65 \times 10^{-3}$ Pa vacuum level, 3.5 times number of cycles, $\geq 1^\circ\text{C}/\text{min}$ average temperature change rate, and ≥ 4 h stable duration at high temperature. Figure 14a shows the typical seven testing points of thermal couplings, where point 2 on the SMPC laminate is the thermal controlling point. Figure 14b shows the actual setup of the thermal vacuum cycling evaluation of SDT without HIMA.

Figure 15 shows the temperature variation of the seven testing points during the thermal vacuum cycling in the space environment simulation equipment. At the high temperature condition in each thermal cycle, the temperature must be maintained for at least 4 h with temperature fluctuation of $\leq 0.5^\circ\text{C}/\text{h}$. The actual vacuum degree was maintained at 6.0×10^{-4} Pa. After this thermal vacuum cycling testing, the appearance and function of the SDT were examined and confirmed to be normal. The electrical conductivity for all the electrical heating films was in the normal range after the thermal vacuum cycling testing. This work mainly focused on the system design of SDT. Another paper will specially discuss the details of the thermal design, including the calculation of the thermal parameters, scheme design, thermal simulation, fabrication processing of HIMA, and the corresponding thermal experimental validation (thermal balance experiments and thermal vacuum cycling).

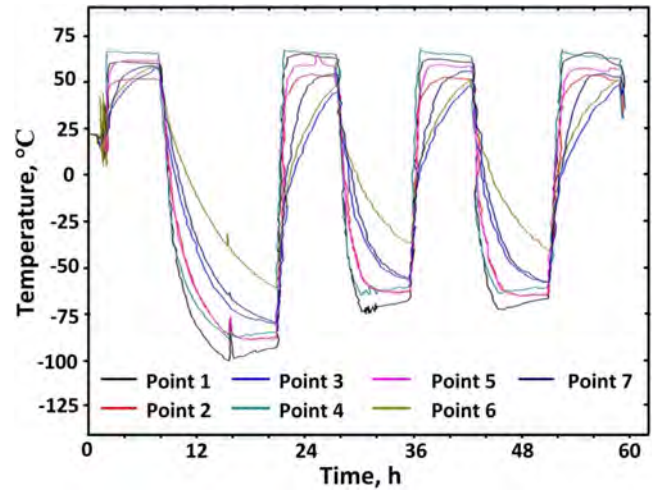
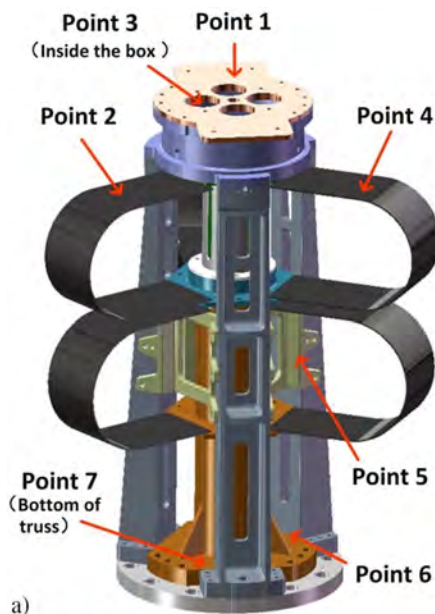


Fig. 15 Thermal cycling curves of the thermal vacuum cycling evaluation of SDT.

C. Locking and Releasing Performance of the SMA Releasing Mechanism

A pretension force of 2000 N could be reliably applied when the titanium nut was torqued with a torque wrench at $6.67 \text{ N} \cdot \text{m}$. The SMA tube was precompressed with approximately 4% strain before being installed on the SMA releasing mechanism. It could increase to 4% length during electric heating due to the shape-memory effect, and the corresponding output force exceeded 10,000 N. In this way, the titanium rod (Fig. 5) would be also forced to increase the length beyond its strain limit and break in the grooving area. Accordingly, the movable parts of the SDT were released. After the breaking of the titanium rod, these released parts were captured by special capturing caps to prevent the formation of space junk because both parts of the separated bolt had a certain amount of kinetic energy.

In this work, the releasing test was carried out four times to evaluate the unlocking and separation functions, and the corresponding vibration shock data of the unlocking process were recorded. The electrical resistivity of a single electrical heating film of the SMA expansion breaker was 20Ω . Upon applying a direct current with 19.6 V and a power of 19.2 W, the SDT was unlocked with an average releasing duration of 30 s. The typical appearance of an unlocked SDT is shown in Fig. 5b-3. Based on the test results, the peak-to-peak

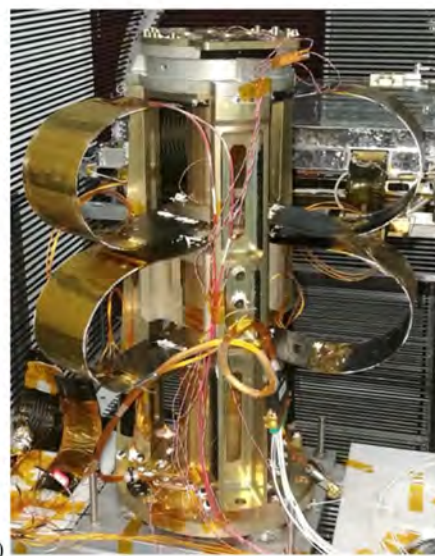


Fig. 14 Thermal vacuum cycling evaluation of SDT without HIMA: a) typical testing points of thermal couplings; b) testing setup of the SDT flight hardware for the SJ18 Satellite.

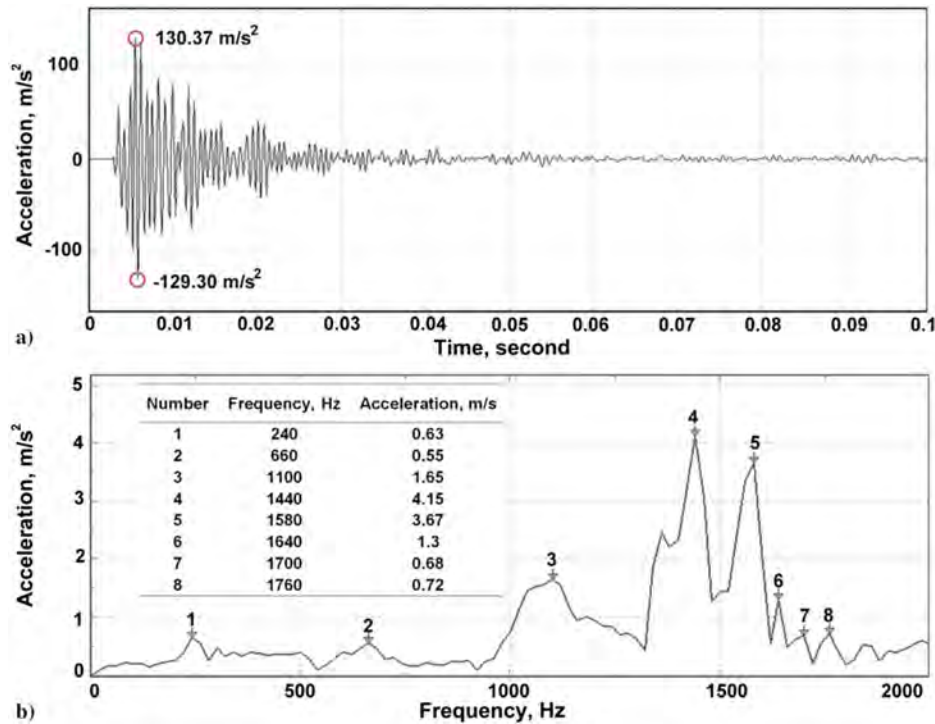


Fig. 16 Typical transient shocking data of the SDT in the unlocking of the SMA releasing mechanism: time domain curve (a) and the corresponding frequency domain curve (b).

values of the vibration acceleration were 259.67 (Fig. 16a), 260.71, 287.09, and 293.87 m/s^2 , with an average value of 275.34 m/s^2 . Hence, the transient shocking value during the unlocking was approximately 14 g . In addition, the vibration shocking duration of the unlocking was approximately 0.02 s. The corresponding frequency domain was obtained, as shown in Fig. 16b, using the fast Fourier transform for the time domain data (Fig. 16a). The first-order natural frequency (240 Hz) should be a local mode of SDT. The second-order natural frequency (660 Hz) correlated well with the first-order natural frequency of the SDT in the Z direction (641–665 Hz; Table 2). The vibration shock of the SMA releasing mechanism in the unlocking process excited the resonance of the SDT in the Z direction.

D. Actuation Performance of the SMPC Laminates

The actuation performance of the cyanate-based SMPC laminates was characterized according to the method in our previous study [18,42]. The resistance of each electrical heating film was 127 Ω . The balance temperature of SDT was approximately 220°C. The evolution

of the actuation force of an SMPC laminate along the axial movement direction of the movable sleeves was studied. In the area of zero recovery angle (i.e., the SMPC in U shape), the recovery force of a single first-stage SMPC laminate was approximately 8–10 N, which provided a relatively large force to trigger the deployment of the SDT. During the recovery process, from the recovery angle 0 to $\sim 60^\circ$, the recovery force linearly decreased to approximately 5 N. The recovery force at the range of recovery angle from 60 to 150° remained at the level of 4–5 N. When the recovery angle was higher than 150°, the recovery force sharply dropped to zero at the recovery angle of approximately 165° (91% recovery ratio). Based on the above recovery behavior, the final recovered angle of the SMPC laminates for the deployed SDT was less than 150° (recovery ratio 83%) to maintain a relatively large recovery force during the whole deploying process. The carbon fiber tow of a fabric-reinforced SMPC underwent a local microbuckling during a bending deformation. Figure 17a shows the microbuckling array of carbon fiber tows on the inner surface of a bending-deformed SMPC laminate undergoing more than 20 deformation cycles. Figure 17b shows an optical image of local microbuckling of a cross-fiber tow unit, and the sinusoidal buckling fibers are evident. As shown in the zoom-in image

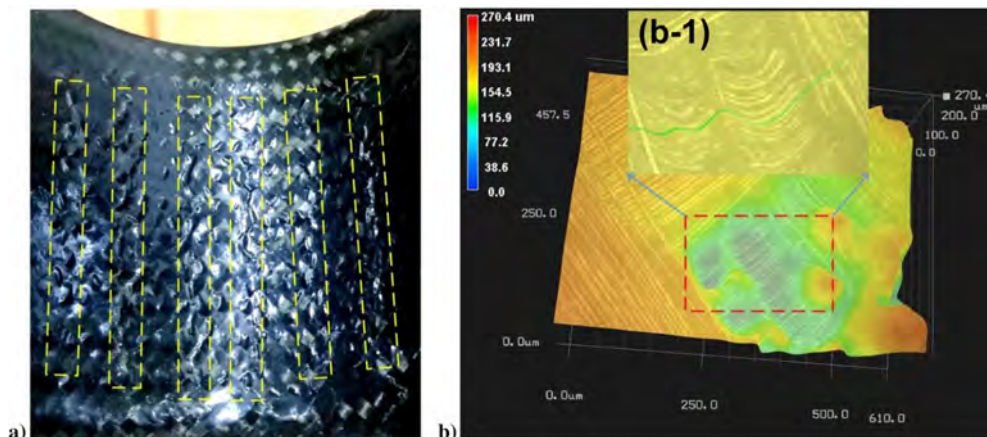


Fig. 17 Microbuckling configuration of a bending-deformed SMPC actuation laminate: a) microbuckling array and b) local microbuckling of a cross-fiber tow.

of Fig. 17b-1, the amplitude is at a magnitude of $100\ \mu\text{m}$, and two cycles of buckling waves could be apparently observed in one repeating cross unit of the twill weaves. The small ratio of the curvature radius to thickness could be achieved and further applied for the large deformation actuation due to these typical microbuckling characteristics of the fabric-reinforced SMPC. Moreover, failures were not observed in the predeformed or recovered configuration within 20 deformation cycles of the SMPC laminates, indicating the engineering applicability of the SMPC for space deployment structures.

In this study, the SMPC combines the functions of structural supporting and mechanism actuation. The SMPC can deform at a 10% macroscale compressive strain due to the large deformation of SMP. The SMP matrix deforms in a large shear strain with the typical microbuckling deformation mode of the reinforced fibers; hence, the SMPC laminate could deform in a small ratio of curvature radius to thickness according to our previous study [20,21]. Moreover, the actuation force of all SDT deployment SMPC laminates decreased from $\sim 30\ \text{N}$ (0°) to $\sim 12\ \text{N}$ (165°) with a recovery duration of approximately 150 s, which was strong enough for the actuation of a space deployable structure in the zero-gravity or microgravity condition. The structural material, structural design, mechanical analysis, and manufacturing of SMPC are almost the same as those of normal fiber-reinforced composites. The structural design standard of the SMPC at the glass state also follows that of the traditional composite mechanics. The stiffness and strength of the SMPC at room temperature are comparable to traditional fiber-reinforced composites, implying that SMPC could be used for most space deployment structures. Furthermore, the preparation processing of SMPC can also employ vacuum bag molding, lamination pressure molding, filament winding process, and resin transfer molding, which are commonly used for fiber-reinforced composites. In summary, the SMPC shows general applicability for new-generation deployable structure in space.

E. Ground-Based Releasing and Deployment Evaluation of SDT

SDT was designed and manufactured, and its performance (structural mechanics, thermal vacuum behavior, locking and releasing of the

SMA releasing mechanism, actuation of the SMPC laminates) was evaluated. Furthermore, the integrated validation of SDT must be conducted according to its complete working procedure. In a simulated weightless environment for SDT, the SMA releasing mechanism was electrically heated and released, followed by the SMPC laminates being electrically heated and actuating the moveable parts to a designed configuration, as shown in Fig. 18.

Two suspension balloons were employed to simulate the zero gravity conditions at an atmospheric temperature of 20°C in air, as shown in Figs. 18a-1 and 18a-2. A ring-shaped suspension balloon was used to offset the gravity of the second-stage sleeve. A lemon-shaped suspension balloon was used to offset the gravity of a third-stage sleeve and a top box. Meanwhile, several circuits of the direct current power were applied to the electrical heating films attached to the SMA releasing mechanism and SMPC laminates. The total heating power of the series electrical heating films of the two SMA expansion breakers was 38.72 W with a resistance of $41.4\ \Omega$. The values of resistance of the electrical heating films attached to the SMPC actuation films were 127.2, 126.9, 127.5, 126.2, 126.8, and $127.2\ \Omega$. A direct current of 100 V was also loaded on each SMPC laminate, and the corresponding values of the heating power for the six pieces of the SMPC laminates were 78.62, 78.81, 78.43, 79.24, 78.86, and 78.62 W. Upon heating, the signal of the microswitch shifted at 28 s, indicating that the SMA releasing mechanism unlocked right at this time. Accordingly, all the moveable parts of the SDT were free in their respective deployment paths. The moveable parts of the SDT quickly deployed vertically up in 29–31 s (Figs. 18b-1–18b-3) due to the relatively large actuation forces in the initial recovery angle 0 to approximately 60° (Fig. 18). Figures 18b-4–18b-6 show the snapshots of deploying configuration at 90, 130, and 180 s. The moveable parts of the SDT were deployed from 30 to 180 s with a relatively slow speed. There are totally six pieces of SMPC laminates, which were divided into two groups for actuation. According to the actuation force ($10\text{--}4\ \text{N}$ during the deployment process) provided in Sec. III.D, the actuation force of all SMPC laminates for SDT deployment decreased from $\sim 30\ \text{N}$ (0°) to $\sim 12\ \text{N}$ (165°). At approximately 180 s, the SDT finally deployed to the designed configuration and self-locked through a lock pin. In 3 min,

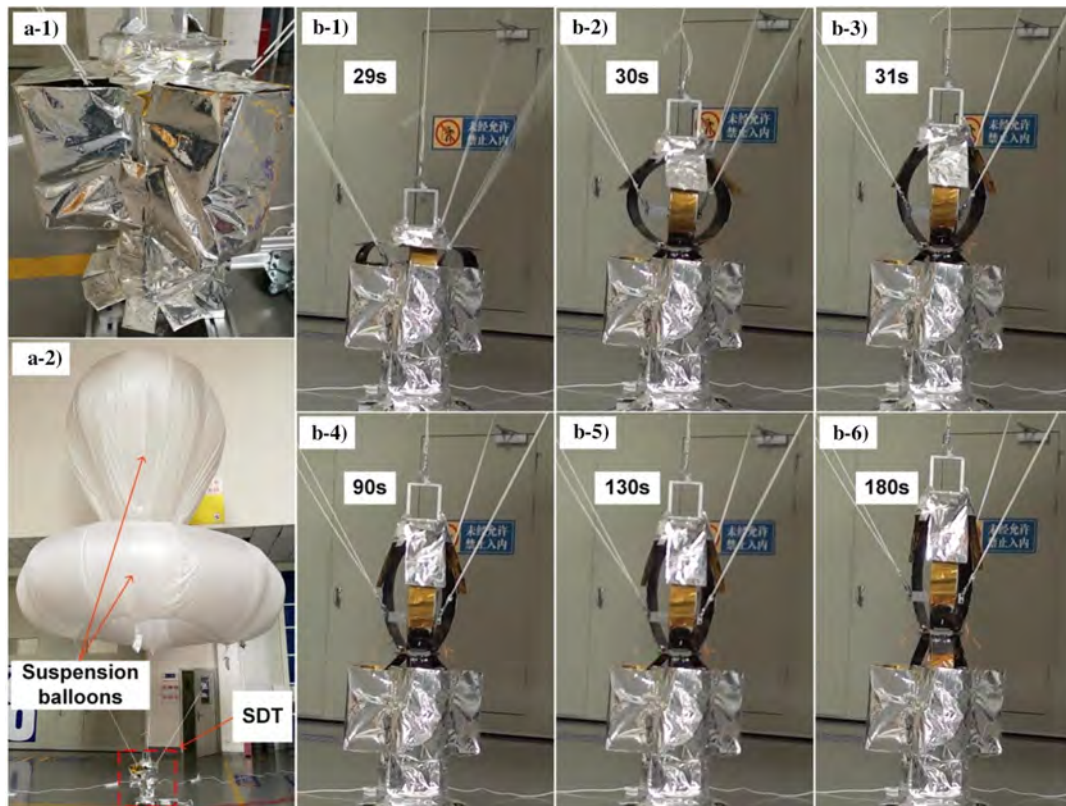


Fig. 18 Ground-based validation of SDT: releasing of the SMA releasing mechanism and deployment of the SMPC actuation laminates.

the SDT realized the releasing of the SMA releasing mechanism and the deployment of the SMPC laminates, which successfully validated the key functions of releasing and deployment of SDT.

The SDT was installed on the outside surface of the east board of the SJ18 Satellite, together with the deployable solar array on the basis of shape-memory materials [44]. This Earth synchronous satellite was launched by Long-March Five Y2 Heavy Rocket on July 2, 2017, at WenChang Satellite Center. In the first 900 s since launching, the SDT structure was intact, and the microswitch was not triggered, indicating that the overall structural design and locking function of the SDT met the harsh requirements of the initial launching stage of a heavy rocket. However, the SJ18 Satellite failed to reach the Earth synchronous orbit (36,000 km) due to the abnormal working state of the Long-March Five Y2 Heavy Rocket. Consequently, the unlocking function of the SMA releasing mechanism and the deployment of the SMPC actuation laminates were not validated on-orbit.

IV. Discussions and Future Prospections

In this work, the SMA releasing mechanism was used to achieve the function of locking and separation, and traditional pyrotechnic devices were not used. The SMA releasing mechanism adopts a lightweight, miniaturized, and integrated design. It exhibits the following advantages: reusable SMA expansion breaker, testable unlocking function, low impact during releasing, no harmful gas or fragments generated by the gunpowder, no anti-electromagnetic interference or static electricity of a pyrotechnic device, simple and miniaturized structure, and low cost. However, it also shows some disadvantages. The temperature and unlocking characteristics are coupled due to the ambient temperature. The temperature in the whole life cycle must be strictly controlled to prevent its accidental unlocking and reliability. The unlocking duration of SMA is long (10–50 s), which is unsuitable for quick unlocking. Furthermore, the unlocking synchronization is poor, and it is unsuitable for occasions that require the release of multiple unlocking devices with accurate synchronization control. The output force of the SMA releasing mechanism is relatively low compared with those of pyrotechnic explosive devices. In summary, SMA releasing mechanisms are mainly suitable to lock small structures in space. The locking and releasing functions for large space structures still depend on traditional pyrotechnic devices.

There are generally two types of SMPs applied in deployed structures or locking/releasing mechanism in space, namely, epoxy-based SMP ($T_g \sim 120^\circ\text{C}$) and cyanate-based ($T_g \sim 170^\circ\text{C}$). Compared with cyanate-based SMP, the epoxy-based SMP shows a relatively lower T_g , elastic modulus, and recovery force. However, its toughness is higher and therefore its deformation limit above T_g is higher. In this way, epoxy-based SMP is usually used for the deployable structures working in an ambient temperature condition less than 80°C (40°C safety margin below its T_g). In contrast, the cyanate-based SMP could be used for deployable structures as well as locking/releasing mechanism working in an ambient temperature condition as high as 130°C (40°C safety margin below its T_g).

The disadvantages of SMPC are unavoidable. First, the electrical heating power of the SMPC is relatively large. The SMPC should be Joule heated to the temperature above the T_g of SMP. The heating power for SMPC used in the deep cooling space is larger than $0.3 \text{ W}/\text{cm}^2$ because the SMPC should be heated above its T_g (epoxy-based SMPC: $T_g \sim 120^\circ\text{C}$; cyanate-based SMPC: $T_g \sim 170^\circ\text{C}$). Considering the area of the SMPC deployment structure, the power required to heat the SMPC might account for a high proportion of the power supply for an aerospace vehicle. Second, the design of the SMPC deployment structure for space production should strictly adhere to the thesis of large deformation of a fiber-reinforced SMPC. However, the large deformation mechanism was primarily developed for a unidirectional fiber-reinforced SMPC, while the thesis for angle-ply or fabric-reinforced SMPC was not yet systematically derived to date. Third, the multistep deployment movement of a large SMPC structure with a long span is difficult to regulate in a desired sequence because its relationship of recovery angle and time is difficult to be accurately controlled.

This work focuses on the systematical introduction of an SDT covering structural design and ground-based experiments (structural strength and vibration, thermal testing, locking and releasing of an SMA releasing mechanism, actuation of SMPC laminates, and deployment validation of SDT). However, the content regarding on-orbit validation of SDT was not included in this work because of the failure of SJ18 Satellite.

V. Conclusions

Several cycles of the optimization design (i.e., structural design, FEA, and ground-based experiment) were carried out to obtain the final form of the SDT flight hardware. The SDT consists of metallic structural frames, three stages of extendable sleeves, six pieces of SMPC actuation laminates, and one SMA releasing mechanism. Its systematical ground-based experiments were conducted, and the overall structural and functional performances met the requirements of the aerospace standards of China for the acceptance level of flight hardware products. The first-order resonance frequency of the SDT in stowed shape was approximately 126 Hz along the axial direction of the extendable sleeves. Considering the locking safety of the SMA releasing mechanism and actuation reliability of the SMPC laminates, the heat insulation multilayer assembly was used to ensure that the local atmosphere temperature of SDT was -100 to $+60^\circ\text{C}$. The limit value of the vibration inertial force of the moveable parts during launching was 500 N. The prestretching force and expansion breaking force for an SMA expansion breaker were ~ 2000 and $\sim 10,000$ N, respectively, to ensure the locking and releasing reliability. The total heating power for the two serial SMA expansion breakers was 38.72 W with a releasing time of 28–30 s. The SMA releasing mechanism of the SDT showed the advantages of reusability, testable unlocking function, and low impact during releasing. The SMPC was used for the actuation for the SDT deployment owing to its 10% macroscale compressive strain. The heating power of the SMPC laminate was 79 W, and the actuation force decreased from 10 to 4 N with a recovery duration of 150 s.

Acknowledgment

This work is supported by the National Natural Science Foundation of China (Grant No. 11632005).

References

- [1] Puig, L., Barton, A., and Rando, N., "A Review on Large Deployable Structures for Astrophysics Missions," *Acta Astronautica*, Vol. 67, Nos. 1–2, July 2010, pp. 12–26.
<https://doi.org/10.1016/j.actaastro.2010.02.021>
- [2] Zhao, J. S., Chu, F. L., and Feng, Z. J., "The Mechanism Theory and Application of Deployable Structures Based on SLE," *Mechanism and Machine Theory*, Vol. 44, No. 2, Feb. 2009, pp. 324–335.
<https://doi.org/10.1016/j.mechmachtheory.2008.03.014>
- [3] Qi, X. Z., Huang, H. L., Li, B., and Deng, Z. Q., "A Large Ring Deployable Mechanism for Space Satellite Antenna," *Aerospace Science and Technology*, Vol. 58, Nov. 2016, pp. 498–510.
<https://doi.org/10.1016/j.ast.2016.09.014>
- [4] Wang, Y., Liu, R. Q., and Yang, H., "Design and Deployment Analysis of Modular Deployable Structures for Large Antennas," *Journal of Spacecraft and Rockets*, Vol. 52, No. 4, July 2015, pp. 1101–1111.
<https://doi.org/10.2514/1.A33127>
- [5] Block, J., Straubel, M., and Wiedemann, M., "Ultralight Deployable Booms for Solar Sails and Other Large Gossamer Structures in Space," *Acta Astronautica*, Vol. 68, Nos. 7–8, April–May 2011, pp. 984–992.
<https://doi.org/10.1016/j.actaastro.2010.09.005>
- [6] Mark, S., Andrew, D. V., Keith, A. S., and Simon, D. G., "Review of Inflatable Booms for Deployable Space Structures: Packing and Rigidity," *Journal of Spacecraft and Rockets*, Vol. 51, No. 3, May 2014, pp. 762–778.
<https://doi.org/10.2514/1.A32598>
- [7] Mallol, P., Mao, H., and Tibert, G., "Experiments and Simulations of the Deployment of a Bistable Composite Boom," *Journal of Spacecraft and Rockets*, Vol. 55, No. 2, March–April 2018, pp. 292–302.
<https://doi.org/10.2514/1.A33906>
- [8] Borowski, E. C., Soliman, E. M., Khan, A. I., and Taha, M. M., "Stowage and Deployment of a Viscoelastic Orthotropic Carbon-Fiber

- Composite Tape Spring," *Journal of Spacecraft and Rockets*, Vol. 55, No. 4, July–Aug. 2018, pp. 829–840.
<https://doi.org/10.2514/1.A33960>
- [9] Fulton, J., and Schaub, H., "Deployment Dynamics Analysis of an Origami-Folded Spacecraft Structure with Elastic Hinges," *Journal of Spacecraft and Rockets*, Vol. 59, No. 2, March–April 2022, pp. 401–420.
<https://doi.org/10.2514/1.A34938>
- [10] Eyer, G., Montagnier, O., Hochard, C., and Charles, J. P., "Effect of Matrix Damage on Compressive Strength in the Fiber Direction for Laminated Composites," *Composites Part A: Applied Science and Manufacturing*, Vol. 94, March 2017, pp. 86–92.
<https://doi.org/10.1016/j.compositesa.2016.12.012>
- [11] Bakis, C. E., Bank, L. C., Brown, V. L., Cosenza, E., Davalos, J. F., Lesko, J. J., Machida, A., Rizkalla, S. H., and Triantafyllou, T. C., "Fiber-Reinforced Polymer Composites for Construction-State-of-the-Art Review," *Journal of Composites for Construction*, Vol. 6, No. 2, May 2002, pp. 73–87.
[https://doi.org/10.1061/\(ASCE\)1090-0268\(2002\)6:2\(73\)](https://doi.org/10.1061/(ASCE)1090-0268(2002)6:2(73))
- [12] Hoos, K. V., Iarve, E., Braginsky, M., Zhou, E., and Mollenhauer, D. H., "Static Strength Prediction in Laminated Composites by Using Discrete Damage Modeling," *Journal of Composite Materials*, Vol. 51, No. 10, May 2017, pp. 1473–1492.
<https://doi.org/10.1177/0021998316651986>
- [13] Ren, P. G., Zhang, Z. P., Xie, L., Ren, F., Jin, Y. L., Di, Y. Y., and Fang, C. Q., "Hybrid Effect on Mechanical Properties of M40-T300 Carbon Fiber Reinforced Bisphenol A Dicyanate Ester Composites," *Polymer Composite*, Vol. 31, No. 12, Dec. 2010, pp. 2129–2137.
<https://doi.org/10.1002/pc.21016>
- [14] Hu, Y. L., and Madenci, E., "Peridynamics for Fatigue Life and Residual Strength Prediction of Composite Laminates," *Composite Structures*, Vol. 160, No. 16, Jan. 2017, pp. 169–184.
<https://doi.org/10.1016/j.compstruct.2016.10.010>
- [15] Li, C. H., and Zuo, J. L., "Self-Healing Polymers Based on Coordination Bonds," *Advanced Materials*, Vol. 32, No. 27, July 2020, Paper 1903762.
<https://doi.org/10.1002/adma.201903762>
- [16] Hegedus, G., Sarkadi, T., and Czigany, T., "Multifunctional Composite: Reinforcing Fibreglass Bundle for Deformation Self-Sensing," *Composites Science and Technology*, Vol. 180, Aug. 2019, pp. 78–85.
<https://doi.org/10.1016/j.compscitech.2019.05.018>
- [17] Forintos, N., and Czigany, T., "Multifunctional Application of Carbon Fiber Reinforced Polymer Composites: Electrical Properties of the Reinforcing Carbon Fibers—A Short Review," *Composites Part B: Engineering*, Vol. 162, April 2019, pp. 331–343.
<https://doi.org/10.1016/j.compositesb.2018.10.098>
- [18] Leng, J. S., Lan, X., Liu, Y. J., and Du, S. Y., "Shape Memory Polymers and Their Composites: Stimulus Methods and Applications," *Progress in Materials Science*, Vol. 56, No. 7, 2011, pp. 1077–1135.
<https://doi.org/10.1016/j.pmatsci.2011.03.001>
- [19] Lendlein, A., and Gould, O. E. C., "Reprogrammable Recovery and Actuation Behaviour of Shape-Memory Polymers," *Nature Reviews Materials*, Vol. 4, No. 2, Jan. 2019, pp. 116–133.
<https://doi.org/10.1038/s41578-018-0078-8>
- [20] Lan, X., Liu, L. W., Liu, Y. J., Leng, J. S., and Du, S. Y., "Post Micro-buckling Mechanics of Fibre-Reinforced Shape-Memory Polymers Undergoing Flexure Deformation," *Mechanics of Materials*, Vol. 72, May 2014, pp. 46–60.
<https://doi.org/10.1016/j.mechmat.2013.05.012>
- [21] Lan, X., Hao, S. D., Liu, L. W., Liu, Y. J., and Leng, J. S., "Macroscale Bending Large-Deformation and Microbuckling Behavior of a Unidirectional Fiber Reinforced Soft Composite," *Journal of Composite Materials*, Vol. 54, No. 2, July 2020, pp. 243–257.
<https://doi.org/10.1177/0021998319854145>
- [22] Liu, Y. J., Du, H. Y., Liu, L. W., and Leng, J. S., "Shape Memory Polymers and Their Composites in Aerospace Applications: A Review," *Smart Materials and Structures*, Vol. 23, No. 2, Feb. 2014, Paper 023001.
<https://doi.org/10.1016/j.pmatsci.2011.03.001>
- [23] Li, F. F., Liu, Y. J., and Leng, J. S., "Progress of Shape Memory Polymers and Their Composites in Aerospace Applications," *Smart Materials and Structures*, Vol. 28, No. 10, Oct. 2019, Paper 103003.
<https://doi.org/10.1088/1361-665X/ab3d5f>
- [24] Taylor, R. M., Abrahamson, E., Barrett, R., Codell, D. E., and Keller, P. N., "Passive Deployment of an Emc Boom Using Radiant Energy in Thermal Vacuum," *48th AIAA/ASME/ASCE/AHS/ASC Structures, Structural Dynamics, and Materials Conference*, AIAA Paper 2007-2269, April 2007.
<https://doi.org/10.2514/6.2007-2269>
- [25] Barrett, R., Francis, W., Abrahamson, E., Lake, M., and Scherbarth, M., "Qualification of Elastic Memory Composite Hinges for Spaceflight Applications," *47th AIAA/ASME/ASCE/AHS/ASC Structures, Structural Dynamics, and Materials Conference 14th AIAA/ASME/AHS Adaptive Structures 7th Conference*, AIAA Paper 2006-2039, 2006.
<https://doi.org/10.2514/6.2006-2039>
- [26] Arzberger, S. C., Tupper, M. L., Lake, M. S., Barrett, R., Mallick, K., et al., "Elastic Memory Composites (EMC) for Deployable Industrial and Commercial Applications," *Smart Structures and Materials 2005: Active Materials: Behavior and Mechanics*, Vol. 5762, International Soc. for Optics and Photonics, San Diego, CA, Jan. 2005.
<https://doi.org/10.1117/12.600583>
- [27] Keller, P., Lake, M., Francis, W., Harvey, J., Ruhl, E., Winter, J., Scherbarth, M., Murphey, T., Barrett, R., and Wintergerst, J., "Development of a Deployable Boom for Microsatellites Using Elastic Memory Composite Material," *45th AIAA/ASME/ASCE/AHS/ASC Structures, Structural Dynamics & Materials Conference*, AIAA Paper 2004-1603, April 2004.
<https://doi.org/10.2514/6.2004-1603>
- [28] Santo, L., Quadri, F., Squeo, E. A., Dolce, F., Mascetti, G., Bertolotto, D., Villadei, W., Ganga, P. L., and Zolesi, V., "Behavior of Shape Memory Epoxy Foams in Microgravity: Experimental Results of STS-134 Mission," *Microgravity Science and Technology*, Vol. 24, No. 4, 2017, pp. 287–296.
<https://doi.org/10.1007/s12217-012-9313-x>
- [29] Santo, L., Quadri, F., Ganga, P. L., and Zolesi, V., "Mission BION-M1: Results of Ribes/Foam2 Experiment on Shape Memory Polymer Foams and Composites," *Aerospace Science and Technology*, Vol. 40, Jan. 2015, pp. 109–114.
<https://doi.org/10.1016/j.ast.2014.11.008>
- [30] Aoki, T., Higuchi, K., and Watanabe, K., "Progress Report of SIMPLE Space Experiment Project on ISS Japan Experiment Module," *Transactions of the Japan Society for Aeronautical and Space Sciences, Aerospace Technology Japan*, Vol. 12, No. 29, 2014, pp. Tc_1–Tc_6.
https://doi.org/10.2322/tastj.12.Tc_1
- [31] Hinkle, J., Cadogan, D., Roushey, J., and Cook, R., "Design and Testing of an Expandable Structure Using Multi-Layer Softgoods Technology," *53rd AIAA/ASME/ASCE/AHS/ASC Structures, Structural Dynamics and Materials Conference*, AIAA Paper 2012-1514, April 2012.
<https://doi.org/10.2514/6.2012-1514>
- [32] Fang, H., Shook, L., John, L., Pearson, J., and Moore, J., "A Large and High Radio Frequency Deployable Reflector," *53rd AIAA/ASME/ASCE/AHS/ASC Structures, Structural Dynamics and Materials Conference*, AIAA Paper 2012-1838, April 2012.
<https://doi.org/10.2514/6.2012-1838>
- [33] Li, F. F., Liu, L. W., Lan, X., Pan, C. T., Liu, Y. J., Leng, J. S., and Xie, Q., "Ground and Geostationary Orbital Qualification of A Sunlight-Stimulated Substrate Based on Shape Memory Polymer Composite," *Smart Materials and Structures*, Vol. 28, No. 7, 2019, Paper 075023.
<https://doi.org/10.1088/1361-665X/ab18b7>
- [34] Zhao, L. H., Wang, H., Chen, G. L., and Huang, S. Z., "Sequentially Assembled Reconfigurable Extended Joints: Self-Lockable Deployable Structure," *Journal of Aerospace Engineering*, Vol. 31, No. 6, 2018, Paper 04018103.
[https://doi.org/10.1061/\(ASCE\)AS.1943-5525.0000877](https://doi.org/10.1061/(ASCE)AS.1943-5525.0000877)
- [35] Zhang, D. D., Zhao, Q. L., Li, F., Tao, J., and Gao, Y. F., "Torsional Behavior of A Hybrid FRP-Aluminum Space Truss Bridge: Experimental and Numerical Study," *Engineering Structures*, Vol. 157, Feb. 2018, pp. 132–143.
<https://doi.org/10.1016/j.engstruct.2017.12.013>
- [36] Otsuka, K., and Makiyama, K., "Deployment Simulation Using Absolute Nodal Coordinate Plate Element for Next-Generation Aerospace Structures," *AIAA Journal*, Vol. 56, No. 3, March 2018, pp. 1–11.
<https://doi.org/10.2514/1.J056477>
- [37] Peffer, A., Fosness, E., Carpenter, B., and Denoyer, K., "On-Orbit Experiments and Applications of Shape Memory Alloy Mechanisms," *Smart Structures and Materials 2000: Industrial and Commercial Applications of Smart Structures Technologies*, Vol. 3991, International Soc. for Optics and Photonics, San Diego, CA, June 2000.
<https://doi.org/10.1117/12.388160>
- [38] Jacobs, S., Coconnier, C., DiMaio, D., Scarpa, F., Toso, M., and Martinez, J., "Deployable Auxetic Shape Memory Alloy Cellular Antenna Demonstrator: Design, Manufacturing and Modal Testing," *Smart Materials and Structures*, Vol. 21, 2012, Paper 075013.
<https://doi.org/10.1088/0964-1726/21/7/075013>
- [39] Maji, A., Mahnke, S. M., and Thomas, W., "Actuation of Neutrally Stable Composite Tape-Springs with Shape Memory Alloy," *Journal of Advanced Materials*, Vol. 41, No. 1, 2009, pp. 18–33.

- [40] Jacobs, S., Coconnier, C., DiMaio, D., Scarpa, F., Toso, M., and Martinez, J., "Deployable Auxetic Shape Memory Alloy Cellular Antenna Demonstrator: Design, Manufacturing and Modal Testing," *Smart Materials and Structures*, Vol. 21, No. 7, 2012, Paper 075013.
<https://doi.org/10.1088/0964-1726/21/7/075013>
- [41] Katsumata, N., Kume, M., and Higuchi, K., "Deployment Behavior Control Using Cables and Bi-Shape Memory Alloy Convex Tape Booms," *Advances in Mechanical Engineering*, Vol. 9, No. 7, 2017, Paper 1687814017707909.
<https://doi.org/10.1177/1687814017707909>
- [42] Li, F. F., Liu, L. W., Du, L. Z., Liu, Y. J., and Leng, J. S., "Mechanical Analysis of a Tip-Loaded Deployable Truss Based on Shape Memory Polymer Composite," *Composite Structures*, Vol. 242, June 2020, Paper 112196.
<https://doi.org/10.1016/j.compstruct.2020.112196>
- [43] Xie, F., Huang, L., Liu, Y., and Leng, J., "Synthesis and Characterization of High Temperature Cyanate-Based Shape Memory Polymers with Functional Polybutadiene/Acrylonitrile," *Polymer*, Vol. 55, No. 23, Nov. 2014, pp. 5873–5879.
<https://doi.org/10.1016/j.polymer.2014.07.035>
- [44] Lan, X., Liu, L. W., Pan, C. T., Li, F. F., Liu, Z. X., Hou, G. H., Dai, W. X., Sun, J., Liu, Y. J., Leng, J. S., Yue, H. H., Zhong, X. Q., Tang, Y., and Xie, Q., "Smart Solar Array Consisting of Shape-Memory Releasing Mechanism and Deployable Hinges," *AIAA Journal*, Vol. 59, No. 6, June 2021, pp. 2200–2213.
<https://doi.org/10.2514/1.J059281>
- [45] Liu, T., Liu, L. W., Yu, M., Li, Q., Zeng, C., Lan, X., Liu, Y. J., and Leng, J. S., "Integrative Hinge Based on Shape Memory Polymer Composites: Material, Design, Properties and Application," *Composite Structures*, Vol. 206, Dec. 2018, pp. 164–176.
<https://doi.org/10.1016/j.compstruct.2018.08.041>